



# Prediction of nanoindentation creep behavior of tungsten-containing high entropy alloys using artificial neural network trained with Levenberg–Marquardt algorithm



Sheetal Kumar Dewangan <sup>a,b</sup>, Ashutosh Sharma <sup>a</sup>, Hansung Lee <sup>c</sup>, Vinod Kumar <sup>b,\*</sup>,  
Byungmin Ahn <sup>a,c,\*\*</sup>

<sup>a</sup> Department of Materials Science and Engineering, Ajou University, Suwon 16499, South Korea

<sup>b</sup> Department of Metallurgy Engineering and Materials Science, Indian Institute of Technology (IIT), Indore 453552, India

<sup>c</sup> Department of Energy Systems Research, Ajou University, Suwon 16499, South Korea

## ARTICLE INFO

### Article history:

Received 25 February 2023

Received in revised form 22 April 2023

Accepted 28 April 2023

Available online 28 April 2023

### Keywords:

High entropy alloy

Powder metallurgy

Indentation creep

Artificial neural network

Machine learning

## ABSTRACT

This paper describes the synthesis of tungsten-containing high-entropy alloys (HEAs). The synthesis method involves a powder metallurgy process, and spark plasma sintering (SPS) is used to compact the powder. XRD and SEM analyses of synthesized HEAs showed that the main phases formed were body-centered and face-centered cubic phases, and a sigma phase was also observed after sintering at 900 °C. Furthermore, nanoindentation showed that the introduction of tungsten in HEA resulted in high hardness and elastic modulus, which ranged from 8.31 to 13.57 GPa and 197.21–209.43 GPa respectively. The indentation creep behavior was ascertained at room temperature. The HEAs exhibited a significant benchmark after the addition of a specific amount of W for further investigation because of their lower creep rate. Experimental creep displacement data were used for modeling by artificial neural networks (ANNs) in which the training has been performed by the Levenberg–Marquardt algorithm. The experimental creep displacement data and the ANN model predictions have an excellent agreement. The ANN model is reliable and can accurately forecast the room temperature creep behavior of HEAs. HEAs are promising candidates for use in elevated and wear-resistance applications, owing to their unique combination of high hardness and high creep resistance.

© 2023 Elsevier B.V. All rights reserved.

## 1. Introduction

Demand for structural materials is increasing day by day because of the only necessity of a high-performance structure for any application. The replacement of multiple parts with a single part always requires a material with excellent structural properties, including good strength and hardness. The strength and properties of any material influence the processing route due to the formation of different microstructures and various parameters. Specifically, powder metallurgy is an essential process for the production of any component. The growth of the powder metallurgy process has extended nowadays, mainly because of three reasons: materials with unique properties can be fabricated, and the process is captivating

and economical. Notably, powder metallurgy techniques facilitate rapid, inexpensive, and high-volume production of precision components [1].

An effective method for mixing and blending alloy powders is mechanical alloying (MA), which is a powder metallurgy technique [2,3]. A solid-state powder manufacturing method called mechanical alloying involves repeatedly welding, breaking, and rewelding. Applying this method to a blended alloy powder yields equilibrium and non-equilibrium alloy phases. The nonequilibrium phases can be combined with a supersaturated solid solution, nanostructures, and metastable crystalline and amorphous alloys. MA is an inexpensive process with huge potential, and it has significant advantages over other mixing and blending methods [4–7]. In the synthesis of new alloys, sometimes, there is no alternative to MA techniques for mixing elements.

After studying different alloy systems, Yeh et al. [8] technologically advanced a new concept of alloy design named high-entropy alloy (HEA). While the conventional alloy system has a minimum of

\* Corresponding author.

\*\* Corresponding author at: Department of Materials Science and Engineering, Ajou University, Suwon 16499, South Korea.

E-mail addresses: [vkt@iiti.ac.in](mailto:vkt@iiti.ac.in) (V. Kumar), [byungmin@ajou.ac.kr](mailto:byungmin@ajou.ac.kr) (B. Ahn).

one principal element system, HEAs, also known as multi-principal-element alloys, contain at least five principal elements, with concentrations ranging from 5 to 35 at%. [8]. Unconventionally, High mixing entropy gives rise to the cocktail effect, slow diffusion, lattice distortions, and the high-entropy effect. The combination of these factors results in the formation of a simple solid solution configuration as opposed to an intricate and intermetallic structure [9]. Many studies have shown that HEAs possess exceptional structural stability, high thermal durability, high oxidation resistance, and superior wear resistance. Owing to these properties, HEAs are potential candidates for a variety of industrial applications [10,11].

Vacuum arc melting is frequently used to produce HEAs, although they can only be used for materials with basic geometry. Arc-melted products have often shown chemical and structural variability. However, powder metallurgy offers many significant advantages over arc melting. In particular, the combination of MA and spark plasma sintering (SPS) has been successfully used for producing unique materials such as superalloys [12]. Processing HEAs by MA results in the HEAs having a more homogenous and stable nanocrystalline microstructure [13] [14].

Recently, Sekhar et al. [15] synthesized TiAlNiCoFe HEA via ball milling and SPS as a single body-centered cubic (BCC) phase. The hardness of the alloy was 700 HV, and its compressive strength was 2.5 GPa. Yurkova et al. (2019) used ball milling and SPS to synthesize AlCuNiFeCr HEA, and they discovered a HEA was in the form of a supersaturated solid solution with a BCC crystalline structure. Interestingly, the alloy comprised three phases after sintering at 800 °C, with a B2 phase being a major phase; the other two phases were a face-centered cubic (FCC) phase and (Cr, Fe)<sub>23</sub>C<sub>6</sub>. The HEA showed high hardness (~ 8.35 GPa) and high compression strength (~ 1960 MPa)[16]. Likewise, Chen et al. described the microstructure along with the mechanical properties of FeNiCrCo<sub>0.3</sub>Al<sub>0.7</sub> synthesized via the same method; a supersaturated solid solution with a BCC structure was observed. However, the partial BCC structure transformed into an FCC structure during SPS. The HEA showed outstanding mechanical properties, namely, yield strength, compression strength, and Vickers hardness; the values of these parameters were 2033 MPa, 2635 MPa, and 624 HV, respectively [17].

One of the techniques which are widely used for assessing mechanical properties is nanoindentation testing. The mechanical characteristics of bulk materials, thin films, and highly brittle materials, which are difficult to create standard specimens, are typically assessed using nanoindentation techniques. The advantage of the nanoindentation approach over the tensile test is the ability to assess the mechanical properties of materials, such as elastic modulus, hardness, and flow stress model parameters, without the need for conventional specimen preparation [18]. Additionally, the succeeding unloading stage can likewise experience creep deformation after the holding stage. A nose-shaped unloading curve may be a direct outcome of this creep deformation during the unloading step. Thus, creep study of the material could be possible through the indentation technique [19–32].

In addition, computational modeling is also used such as molecular dynamics (MD) [33,34] and ANN (artificial neural network) for different properties prediction of the materials [35,36]. However, an artificial neural network (ANN) is an excellent technique to predict the physical properties that could be seen in several reported articles. Recently, these techniques have been applied for the prediction of the crystallite size and lattice parameter of HEA powder which is processed by the powder metallurgy route [37]. Moreover, several studies have been made to predict the different physical and mechanical behavior of a material. It is common knowledge that microstructure has a significant impact on how a material behaves under various strain paths [38,39]. Using ANN approaches, research has been conducted to link the flow characteristics to the microstructure. Thus, researchers used ANN to make reasonable

predictions of stress-strain and texture evolution of polycrystalline materials [40].

Currently, pure elements like i.e., Al, Cr, Fe, Mn, and Ni are widely used in the synthesis of HEAs. By contrast, refractory metals such as Nb, Ta, Mo, V, and W are rarely used in HEAs. The unique properties of refractory metals including high strength and poor ductility could be seen [41,42]. Yong et al. discovered that adding W to alloys such as Fe-based superalloys strengthened the solid solution [43]. In this study, HEAs, namely AlCrFeMnNiW<sub>x</sub> ( $x = 0, 0.05, 0.1, \text{ and } 0.5$ ), were prepared by ball milling and subsequent SPS, and the consequence of the addition of tungsten on the mechanical properties and creep behavior of the HEAs was examined. Additionally, an artificial neural network (ANN) model was established for predicting the creep behavior of the HEA systems.

In materials design and discovery, artificial neural networks are primarily used to address regression, classification, and probability estimation issues. Additionally, ANN performs well in addressing problems involving correlation and prediction. As a result, the use of ANN approaches in materials science can still be broadened to address more issues and is likely to lead to even further advancements. In addition, The study successfully illustrates the usefulness of the ANN model for predicting material behavior under the creep loading condition. It can be also evaluated for the same HEAs if the parameter could be changed after the trained model has been created. Eventually, The predicted capability of the developed model also provides the freedom to choose the HEA composition with the required properties of HEA without any experimental trials.

Eventually, when compared to experimental methods with ANN techniques, ANN provides a significantly reduced time and cost to identify the creep behavior of the alloy other than the excellent fit with the experimental result. This study presents a compression of experimental results and an ANN-based model trained with the Levenberg–Marquardt algorithm to forecast nanoindentation creep behavior for a wide range of materials belonging to the Al, Cr, Fe, Mn, Ni, and W elements.

## 2. Materials and methods

Initially, the 20 h-milled high-entropy alloy powder was sintered using spark plasma sintering (Dr. Sinter S625) at 900 °C with a holding duration of 5 min, a heating rate of 100 °C/min, as well as a pressure of 50 MPa. The sintered sample was examined using scanning electron microscopy (SEM) and X-ray diffraction (XRD). XRD (Bruker D2 PHASER with a Cu radiation target) was used for phase characterization, and an SEM was used for determining the microstructure (JSM 7610 F Plus, JEOL, Japan, and Nova, NanoSEM 450); the microscope was used in the backscattered mode at 20 kV. The authors' previous paper provides details of the HEA synthesis procedure [44].

To find out how the alloy behaved at the nanomechanical level, a nanoindentation test was conducted. The Hysitron Triboindenter (TI 750), which had a Berkovich indenter having a tip radius of 150 nm, was used for all of the nanomechanical research. Open-loop and displacement control modes (loading-holding-unloading) along with a single cycle indentation testing technique were used for the indentation test purpose. In 30 m × 30 m arrays, a minimum of nine indentation points were chosen to preserve acceptable output data correlation, and a minimum of 15 m was maintained between each point. The maximum load in the test was 5000 μN, and the loading rate was 250 μN/s. A dwell time of 10 s was chosen for the indentation creep study. The calibration was performed before the test, and it was ensured that no error occurred because of the indenter tip and machine operation. Average values were obtained to plot the load-displacement curve for further study. Archimedes' principle has been employed to estimate the density of the HEAs.

## 2.1. Input parameters and collection of a dataset for neural network modeling

For the input of the model, it is to be noted that the composition of each HEA is taken in the weight percentage. Further, all the HEAs were used from the present work for making the dataset. The composition of the alloys, the load applied, and the holding time during the indentation test is considered input parameter while indentation depth was an output for developing the ANN model. Thus, the experimental dataset was used for training the neural network. From the experimental results of each alloy system, data on constant load dwell time during creep were obtained and used for modeling.

## 3. Thermodynamic calculations and thermo-calc simulation

A parameter,  $\Omega$ , was proposed in an earlier study to define the mutual influence between  $\Delta H_{\text{mix}}$  and  $\Delta S_{\text{mix}}$ . It provides a standard for the estimate of phase development while synthesizing the high entropy alloy [45] with  $n$  elements, and it can be described by the relationship below. [46]:

$$\Omega = \frac{T_m \Delta S_{\text{mix}}}{|\Delta H_{\text{mix}}|} \quad (1)$$

$$\Delta H_{\text{mix}} = \sum_{i=1}^n \Omega_{ij} c_i c_j \quad (2)$$

where  $\Delta H_{\text{mix}}$  is the mixing enthalpy of binary alloys and  $\Omega_{ij}$  ( $\Omega_{ij} = 4\Delta H_{\text{mix}}^{AB}$ ) is a parameter for the regular melt interaction between the  $i$ th and  $j$ th elements,

On the basis of Boltzmann's hypotheses, the mixing entropy of  $n$  elements  $\Delta S_{\text{mix}}$  can be expressed as

$$\Delta S_{\text{mix}} = -R \sum_{i=1, i \neq j}^n (c_i \ln c_i) \quad (3)$$

Where  $R$  is a gas constant ( $8.314 \text{ J K}^{-1} \text{ mol}^{-1}$ ) and  $c_i$  is a molar fraction of the mixing components.

The melting temperature  $T_m$  of the  $n$ -element alloy can be calculated from the relation

$$T_m = \sum_{i=1}^n c_i (T_m)_i \quad (4)$$

where  $(T_m)_i$  is the melting point of the  $i$ th component of the alloy. The atomic size difference ( $\delta$ ) is a critical parameter for phase formation, and it is given by

$$\delta = 100 \sqrt{\sum_{i=1}^n c_i \left(1 - \frac{r_i}{\bar{r}}\right)^2} \quad (5)$$

Here,  $\bar{r}$  is the average atomic radius of the alloying elements, and it is calculated using the relation  $\bar{r} = \sum_{i=1}^n c_i r_i$ .

The valence electron concentration (VEC) determines whether a BCC or FCC structure will develop. The quantitative prediction of the microstructure (BCC / FCC) of an  $n$ -element alloy was covered by Guo et al. in 2011 [47]. The relationship between both the VEC as well as the concentration of  $n$ -component elements.

$$VEC = \sum_{i=1}^n c_i (VEC)_i \quad (6)$$

For comprehending the nature (complexity) as well as the development of the disordered solid solution within multi-component alloys, a geometric parameter ( $\Lambda$ ) is also important. This parameter can be calculated by [48].

$$\Lambda = \frac{\Delta S_{\text{mix}}}{\delta^2} \quad (7)$$

**Table 1**  
Estimated thermodynamic properties of different HEAs.

HEA	$\Delta H_{\text{mix}}$ (KJ mol <sup>-1</sup> )	$\Delta S_{\text{mix}} \times R$ (J K <sup>-1</sup> mol <sup>-1</sup> )	$T_m$ (°C)	$\Omega$	$\delta$ (%)	VEC	$\square$ (J mol <sup>-1</sup> K <sup>-1</sup> )
AlCrFeMnNiW <sub>x</sub>							
$x=0$	- 6.56	1.61	1361	3.33	5.385	5.20	0.461
$x=0.05$	- 3.92	1.64	1380	5.62	5.397	5.16	0.459
$x=0.1$	- 2.99	1.67	1399	7.75	5.398	5.13	0.459
$x=0.5$	- 2.82	1.76	1540	9.42	5.399	4.91	0.459

**Table 1** displays the calculated physiochemical and thermal parameters, in which  $\Omega$  values increase with  $W$ , as determined by the aforementioned formulae. It is methodically shown in a graph in Fig. 1(a and b). The continual increase of the  $\Omega$  concerning  $W$  contains carries an indicator for the actively forming solid solution. Similarly, the  $W$  addition causes the  $\delta$  value to fall, which increases the solid solution's lattice distortion energy.

In order to predict phase formation, thermodynamic simulations of AlCrFeMnNiW<sub>x</sub> ( $x = 0$  and  $0.5$ ) were performed using the TCHEA2 database and Thermo-Calc® software. Phase fraction-temperature curves for AlCrFeMnNiW<sub>x</sub> ( $x = 0, 0.5$ ) are shown in Fig. 2(a and b). BCC B2 (1), as well as BCC B2#2 (2), was formed from the liquid phase for the AlCrFeMnNiW<sub>x</sub> HEA with  $x = 0$ , whereas a sigma phase ( $\sigma$ ) developed during the solid-state transition. Similarly, in the AlCrFeMnNiW<sub>x</sub> HEA with  $x = 0.5$ , BCC B2 (1) and BCC B2#2 (2) phases were formed from the melt state, while the other phases, such as a sigma phase ( $\sigma$ ), a MU PHASE, and a MU PHASE#2, were formed throughout the solid-state transition [49].

## 4. Results and discussion

**Fig. 3** depicts XRD patterns of the powder HEAs after 20 h of milling and sintered samples. In the powder sample, dissolution of alloying elements was first observed in the powder sample. The instance and a single peak were observed after 20 h of milling. An isolated intense peak confirmed the solid solution phase formation. The milling process mainly involved breakage and cold welding of powder particles, which could lead to mechanical alloying. The BCC phase in the HEA powder was observed mainly after the milling hour, and BCC phase formation was observed even after the addition of  $W$  to the alloy system. After SPS, the HEAs showed several additional phases, such as the sigma ( $\sigma$ ) phase and minor FCC phases. The BCC phase consisted of an AlFe-type phase (JCPDS: 00 – 033–0020; lattice constant = 290.37 pm), and the FCC phase comprised Cr-, Mn-, and Ni-rich phases. A similar work by the same authors could be referred to regarding the phase evolution in the HEAs. For more detailed information [44]. The addition of tungsten was found to significantly affect phase formation in the HEAs.

**Fig. 4(A–D)** depicts SEM images of AlCrFeMnNiW<sub>x</sub> HEAs ( $x = 0, 0.05, 0.1$ , and  $0.5$ ) after 20 h of milling, and 4(A1–D1) shows the morphology of HEA powders after sintering at 900 °C. The HEAs showed two different phases which are AlFe-type and Cr-rich phases. Moreover, the sintered HEAs showed the additional presence of a sigma phase. It is very obvious from the sigma phase, which was formed mainly because of the presence of chromium. However, in the present study, mechanical alloying did not result in the formation of oxide or carbide. A more detailed discussion of the different phases is presented in the authors' previous paper [44].

The Oliver and Pharr method was used to determine the modulus of elasticity and hardness [50]. **Fig. 5(a)** shows a plot of the load against the displacement, and **Fig. 5(b)** displayed a chart with the estimated value. Initially, the HEA AlCrFeMnNiW<sub>x</sub> ( $x = 0$ , without tungsten added) had reasonable hardness and elastic modulus. These values decreased with the addition of tungsten, probably because of a decrease in the fraction of the sigma ( $\sigma$ ) phase in the HEA.

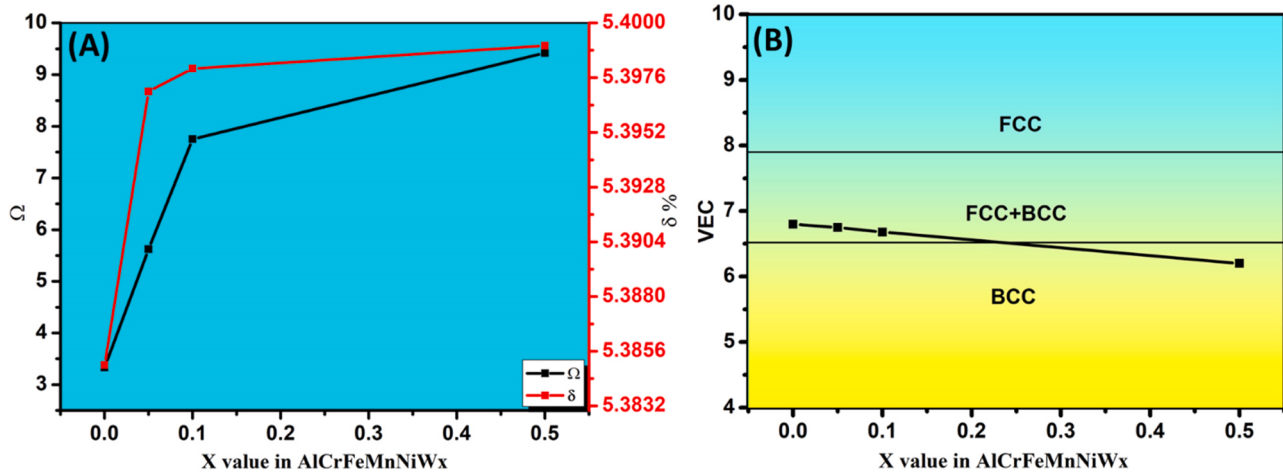


**Fig. 1.** (a) Plots of  $\Omega$  and  $\delta$  against the tungsten content and (b) the relationship between the VEC and the W content of the alloy.

Further addition of tungsten improved the hardness and elastic modulus in the HEAs. It is hypothesized that three significant factors, which play a significant role in the strengthening mechanism of any alloy, may have contributed jointly to the HEAs' high hardness: the grain size, grain boundary, and precipitate hardening [51,52].

Since the hardness of the different phases was investigated extensively in the present study, a hardness distribution contour map could help understand the hardness range of present phases. Hence, a hardness distribution plot obtained for nine indents in a  $30 \mu\text{m} \times 30 \mu\text{m}$  array was prepared, and it is shown in Fig. 6. In the investigated HEAs, XRD analysis confirmed the existence of three phases: BCC (hard phase), FCC (soft phase) [53], and  $\sigma$  (very hard phase) [54] phases. On the basis of the significant characteristic of the phases, it could be concluded that the region in red and shown by dark color is harder because of the presence of the  $\sigma$  phase. The BCC and FCC phases were comparatively less hard than indicated by the color map. The hardness on the surface of the HEAs could be accurately measured. In particular, the densification of the HEAs after sintering significantly influenced the hardness evaluation. The HEAs with  $x=0.1$  had the highest hardness, possibly because they had the highest relative density among all the HEAs.

Usually, alloys prepared through mechanical alloying and subsequent SPS have high hardness compared with alloys prepared

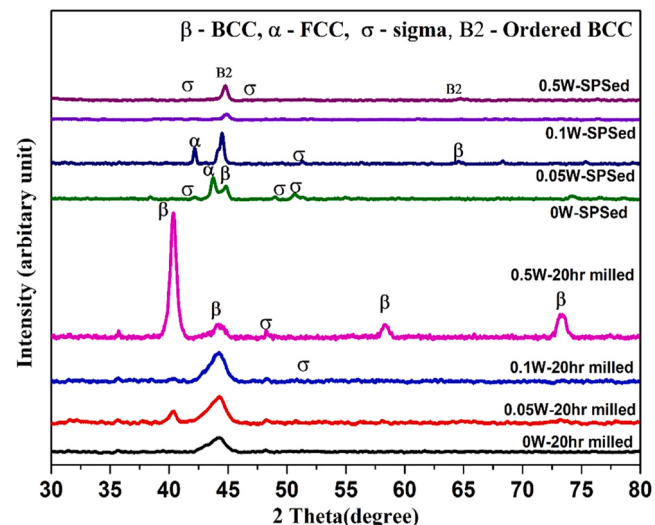


**Fig. 3.** Diffraction patterns of milled powder and sintered  $\text{AlCrFeMnNiW}_x$  ( $x = 0, 0.05, 0.1$  and  $0.5$  mol) HEAs.

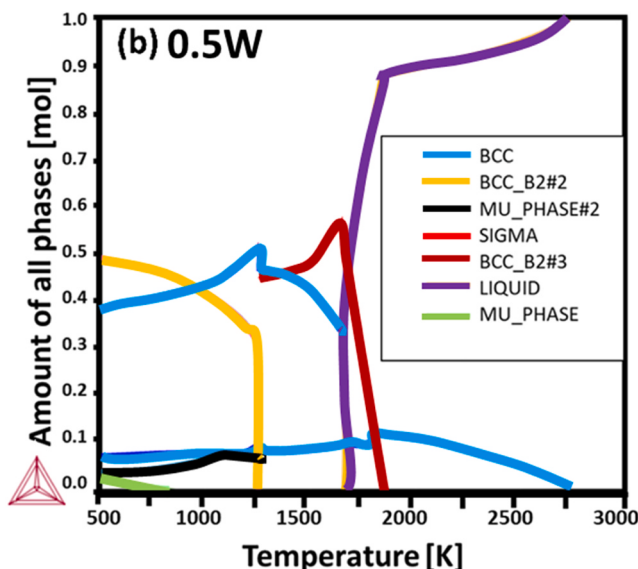
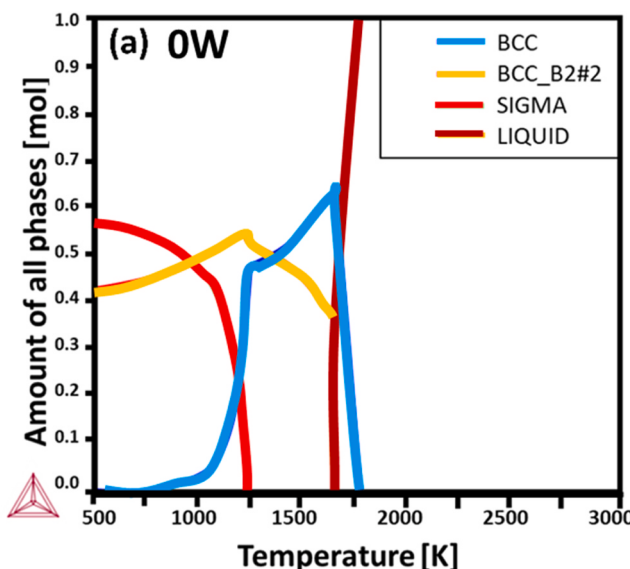


**Fig. 2.** Results of thermodynamic simulations of  $\text{AlCrFeMnNiW}_x$  HEAs with (a)  $x = 0$  and (b)  $x = 0.5$ .

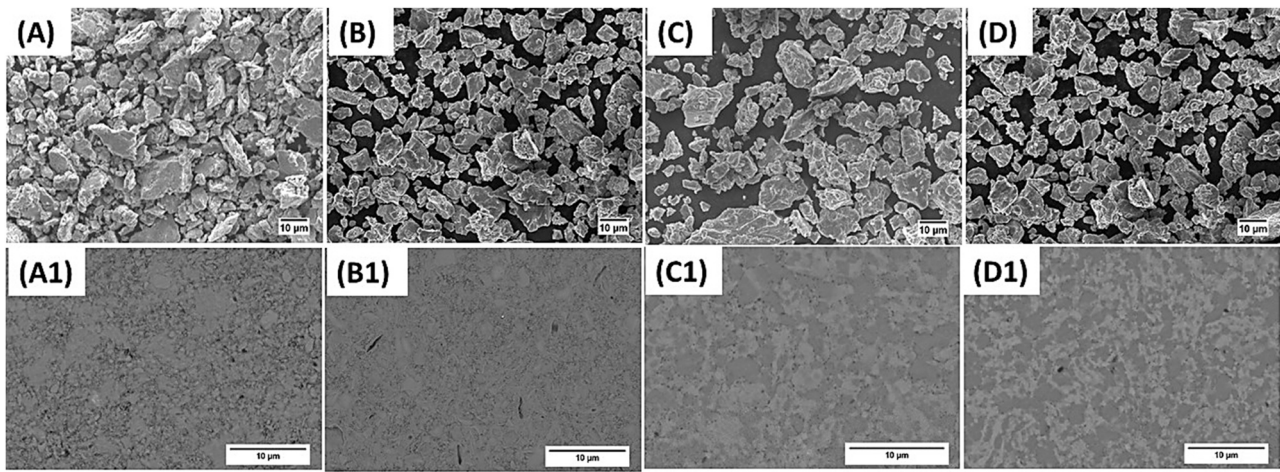


**Fig. 4.** SEM images of (A–D) ball-milled and (A1–D1) sintered  $\text{AlCrFeMnNiW}_x$  ( $x = 0, 0.05, 0.1$ , and  $0.5$ ).

using other processing routes i.e., arc melting. Comparable values for the nano hardness and modulus of elasticity have been observed in  $\text{AlCoCrCuFeNi}$ , namely  $8.13 \pm 0.15$  GPa and  $172 \pm 10$  GPa, respectively [55]. Furthermore, nanocrystalline  $\text{CrMnFeCoNi}$  HEA film also has a high hardness of 11.1 GPa.

The rule of the mixture (Eq. 10) and the Archimedes principle were used to calculate the experimental and theoretical densities of  $\text{AlCrFeMnNiW}_x$  HEAs with  $x = 0, 0.05, 0.1$ , and  $0.5$ . The variation of the density, elastic modulus, and hardness of the various HEAs with the W content is depicted in Fig. 5(b).

$$p_{\text{mix}} = \frac{\sum c_i A_i}{\sum \frac{c_i A_i}{p_i}} \quad (8)$$

Indentation creep tests were performed to understand the mechanical behavior of the material. The creep phenomenon can be defined as an increase in the penetration depth under constant load. In the creep test, the selected final load was maintained constant for a specific period and the indentation depth was then measured. Plastic deformation occurred during the holding period, and it could not be completely reversed. The experimental dimensional change was mainly because of creep. The role of elasticity can be neglected in studies of creep at room temperature. Measuring the creep plastic deformation with a Berkovich indenter when the amount of stress is

very small can provide clues to the mechanism underlying the deformation [56]. Creep data obtained from an indentation experiment can be analyzed by the empirical equation

$$h = h_0 + a(t - t_0)^b + kt \quad (9)$$

where  $h$  is the indenter displacement at a given time  $t$ . The parameters  $t_0$  and  $h_0$  are the initial holding time and displacement at the peak load, respectively, and  $a$ ,  $b$ , and  $k$  are the fitting parameters. The holding time and displacement are related, and they can be calculated by fitting a curve. Since the experiment dataset had a small amount of noise because of the short holding period, a satisfactory correlation was developed between the holding time and displacement ( $R^2 > 0.85$  for all tests). The fitting parameters and the experimental dataset are shown in Fig. 7(a, b, c, and d). Two common primary and secondary stages of nanoindentation are also observed as shown in Fig. 7(a), (b), (c), and (d). The creep displacement upsurges rapidly while the creep rate decreases speedily at the primary stage. The creep displacement increases almost linearly with the holding time, and the creep rate remains constant at the secondary stage.

In Fig. 8, the two stages in the creep deformation curve are the primary stage creep and the secondary stage steady-state creep. In the primary stage, the creep displacement acts rapidly while the

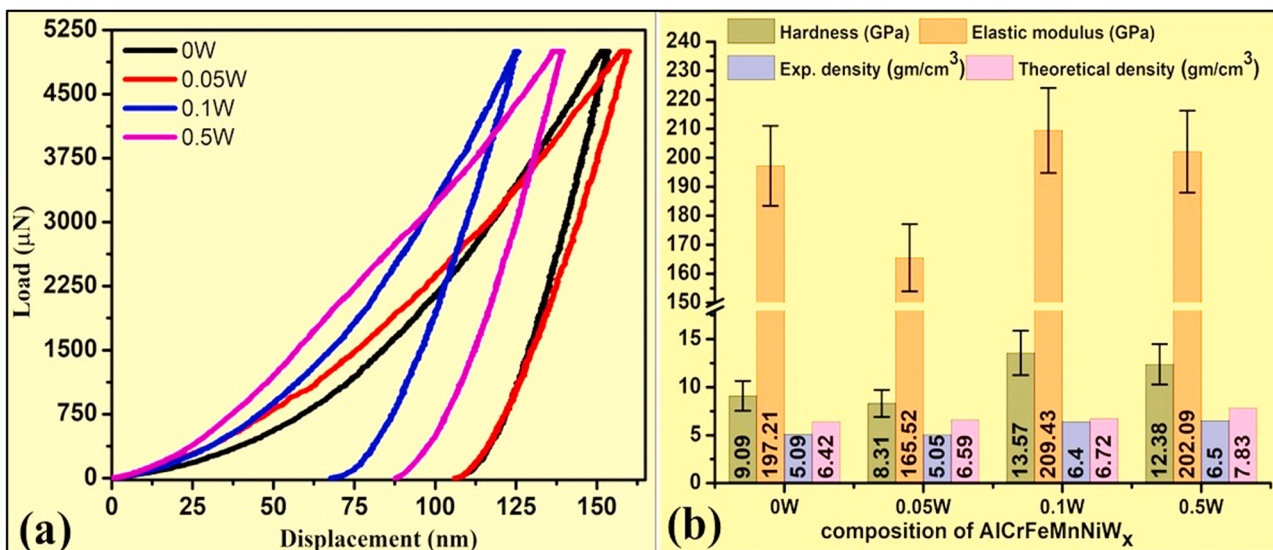


**Fig. 5.** Presentation of (a) load vs. displacement curves and (b) hardness and elastic modulus of HEAs.

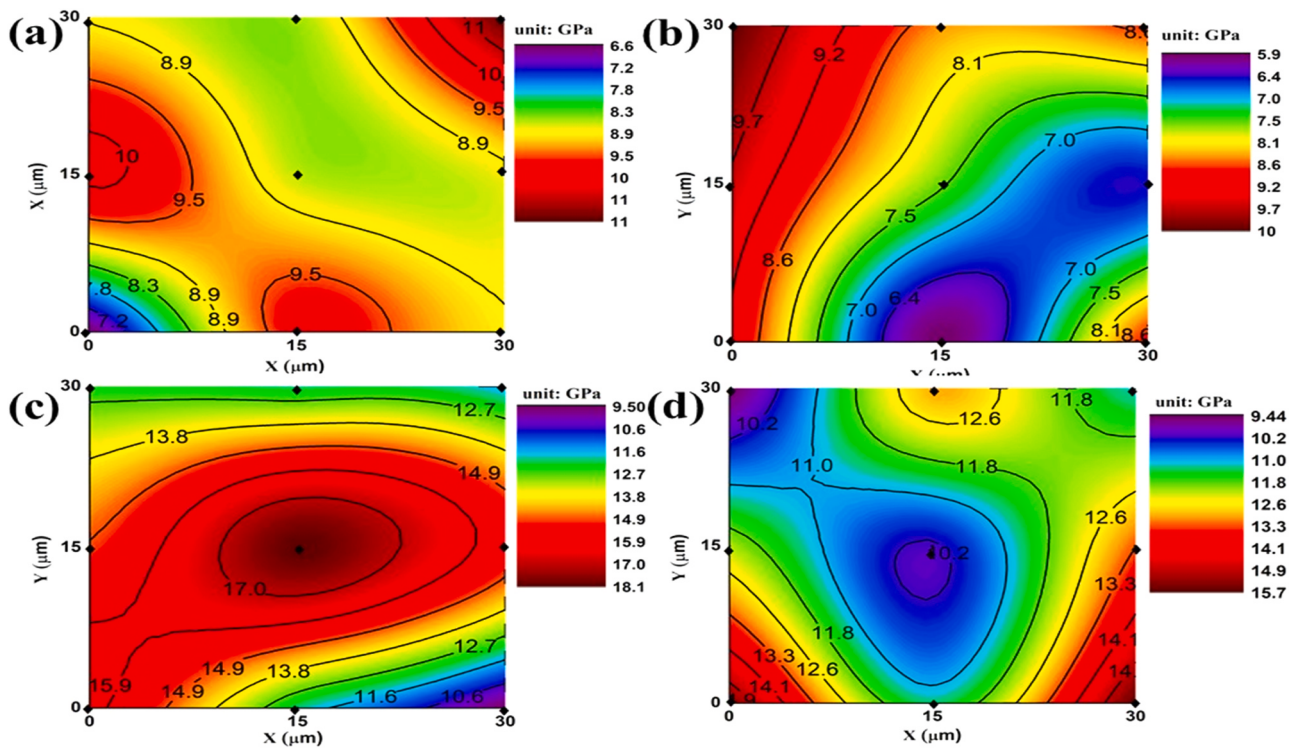


**Fig. 6.** Representation of hardness distribution in a 30 μm × 30 μm array with nine indent points of the AlCrFeMnNiW<sub>x</sub> HEAs: (a) x = 0, (b) x = 0.05, (c) x = 0.1, and (d) x = 0.5.

creep rate performs slowly. After some time, the curve enters a steady-state zone and the creep displacement becomes somewhat linear, and eventually, the creep rate increases and reaches a stable level. The vertical line marks the separation between the two stages in Fig. 9. Unlike the classical creep curve, they do not have the third stage because the material cannot fail catastrophically during the indentation experiment at very low stress [56]. In the current study, an intense creep displacement was evident, and a rapid decrease in the creep rate was observed. A high creep rate was observed at the primary stage, and it ranged from about  $5 \times 10^{-3}$  to about  $2.5 \times 10^{-4}$  for all HEAs, except that with  $x = 0.05$ .

Owing to the continuous reduction in the creep strain in the HEA, it was difficult to identify the primary stage limit. The alloy had a moderate creep rate in the steady-state region, similar to the classical creep curve. The creep rate ranged between  $1.5 \times 10^{-3}$  and  $2 \times 10^{-3}$  in the steady-state stage.

Doerner and Nix [57] proposed the following significant empirical relation between creep strain rate  $\dot{\epsilon}$  and displacement:

$$\dot{\epsilon} = \frac{1}{h} \frac{dh}{dt} \quad (10)$$

Fitting a curve to a plot of the creep strain rate vs. displacement can help determine the creep strain rate from Eq. (9). Furthermore, the creep strain rate obtained by differentiating the equation concerning time is shown in Fig. 8.

Fig. 8 also shows the indentation creep displacement plotted against the holding time at the maximum loading condition for 10 s. The creep behavior of all samples was more similar in the given period of investigation. In every creep experiment, the displacement was high at the beginning of the holding period up to the steady state, and it reached a saturation level at a later stage. It was also noticed that the creep deformation was higher for a larger load [56]. A strong relationship was observed between the creep movement

and the holding time. Furthermore, the creep displacement and creep rate increased with the holding time. The creep curve was drawn from zero for both displacement and time for a better explanation. The HEA showed excellent creep resistance, which is significantly correlated to the hardness, modulus of elasticity, and creep behavior.

The empirical power law equation is followed by the self-similar indentation creep [58]:

$$\dot{\epsilon} = A\sigma^{\frac{1}{m}} \exp(Q/RT) \quad (11)$$

Here, A is a constant, Q is the activation energy, and m is the creep strain rate sensitivity parameter. The relationship between the hardness gradient (H) and strain can be expressed as

$$\dot{\epsilon} = -\beta \frac{1}{H} \frac{dH}{dt}, H = c\sigma \quad (12)$$

where  $\beta$  and c are parameters related to the indenter and material, respectively. The following relation can be used to estimate the indentation hardness,

$$H_i = \frac{P}{24.56h^2} \quad (13)$$

where  $H_i$  is the indentation hardness, P is the peak load during the creep study, and h is the indentation displacement.

Substituting Eq. (12) in Eq. (11) and integrating both sides with respect to time yields the following relationship between the hardness of the creep and the holding time. Eventually, a relationship has developed between the hardness of the creep and the holding time. It could be presented as.

$$\frac{1}{m} \ln H = \ln \left( \frac{An}{\beta c^{\frac{1}{m}}} \right) - \frac{Q}{RT} + \text{Int} \quad (14)$$

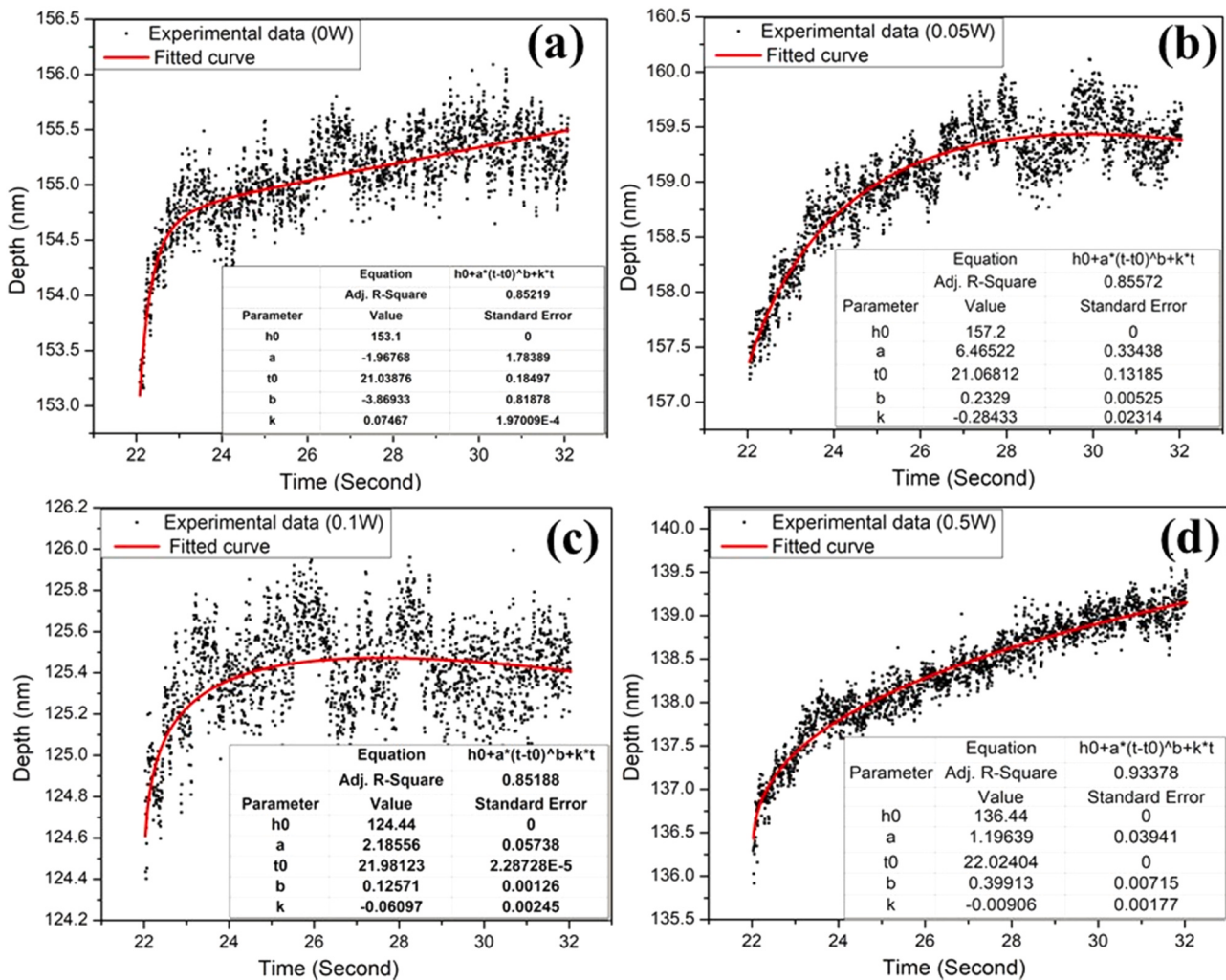


**Fig. 7.** (a) Total creep displacement as a function of the holding time with fitting parameter of the AlCrFeMnNiW<sub>x</sub> HEAs: (a) x = 0, (b) x = 0.05, (c) x = 0.1, and (d) x = 0.5 (characterized by the indenter depth).

The value  $\frac{A_n}{\beta C^{1/m}}$  is a structure-dependent constant.

By taking the double logarithm of both sides of Eq. (14) and constructing a plot of the hardness vs. the holding time, we can obtain the value of  $m$ ; the plot is shown in Fig. 9. The slope of the plot indicates  $m$ . The value of  $m$  was calculated at the peak load and loading rate of 5000  $\mu$ N and 250  $\mu$ N/s, respectively, and the AlCrFeMnNiW<sub>x</sub> HEAs ( $x = 0, 0.05, 0.1$ , and  $0.5$ ) had values of  $7.3 \times 10^{-3}$ ,  $4.8 \times 10^{-3}$ ,  $2.5 \times 10^{-3}$ , and  $7.98 \times 10^{-3}$ , respectively. A similar value of strain rate sensitivity exponent has been reported for CoCrFeMnNi HEA and Al<sub>0.1</sub>CoCrFeNi, with the values being in the approximate range of  $7 \times 10^{-3}$  to  $60 \times 10^{-3}$  [59]. Furthermore, TiZrHfBCu HEB-MG has comparable values of  $m$  for different loading conditions, ranging from about  $6 \times 10^{-3}$  to  $9.61 \times 10^{-3}$  [60]. Previous work has shown that  $m = 1$  implies Newtonian flow and  $m < 1$  indicates inhomogeneous non-Newtonian flow. Accordingly, the moderately low value of  $m$  can be ascribed to strongly localized shear flow. Noticeably, the value of  $m$  of the investigated HEAs was also lower than that of crystalline metallic materials and HEAs, such as Ni-based alloys ( $m = 0.018$ – $0.058$ ) and AlCoCrCuFeNi HEA ( $m = 8 \times 10^{-3}$  at a load of 8000  $\mu$ N) [55]. A higher value of  $x = 0.1$  ( $2.15 \times 10^{-3}$ ) is affected by the solid solution, which is reflected in hardness and strain rate sensitivity [61].

## 5. ANN prediction of the creep behavior of HEAs

A model that can predict the real creep performance of alloy systems against the experimental nanoindentation and it could be built in order to understand how an alloy behaves owing to alloying components. A neural network that can be used to solve issues in the actual world may be created for this purpose. The indentation depth served as an output parameter, and the alloying mixture, applied load, and holding time were chosen as input factors. As a result, the experimental dataset was used for training the neural network. From the experimental results of each alloy system, data on constant load dwell time during creep were obtained and used for modeling. The dataset was further divided into three portions for training, validation, and testing in the proportions of 70%, 15%, and 15%, respectively, during the simulation of the model.

The input, hidden, and output layers of an ANN model are shown in Fig. 10(b). The neurons that make up each layer are individual components whose communication is determined on the basis of their weights. The neurons transmit a variety of information via signals, which are transmitted from one neuron to the next neuron, to modify the weight. A backpropagation method has also been used, and it is known to accurately predict material characteristics. Hence,

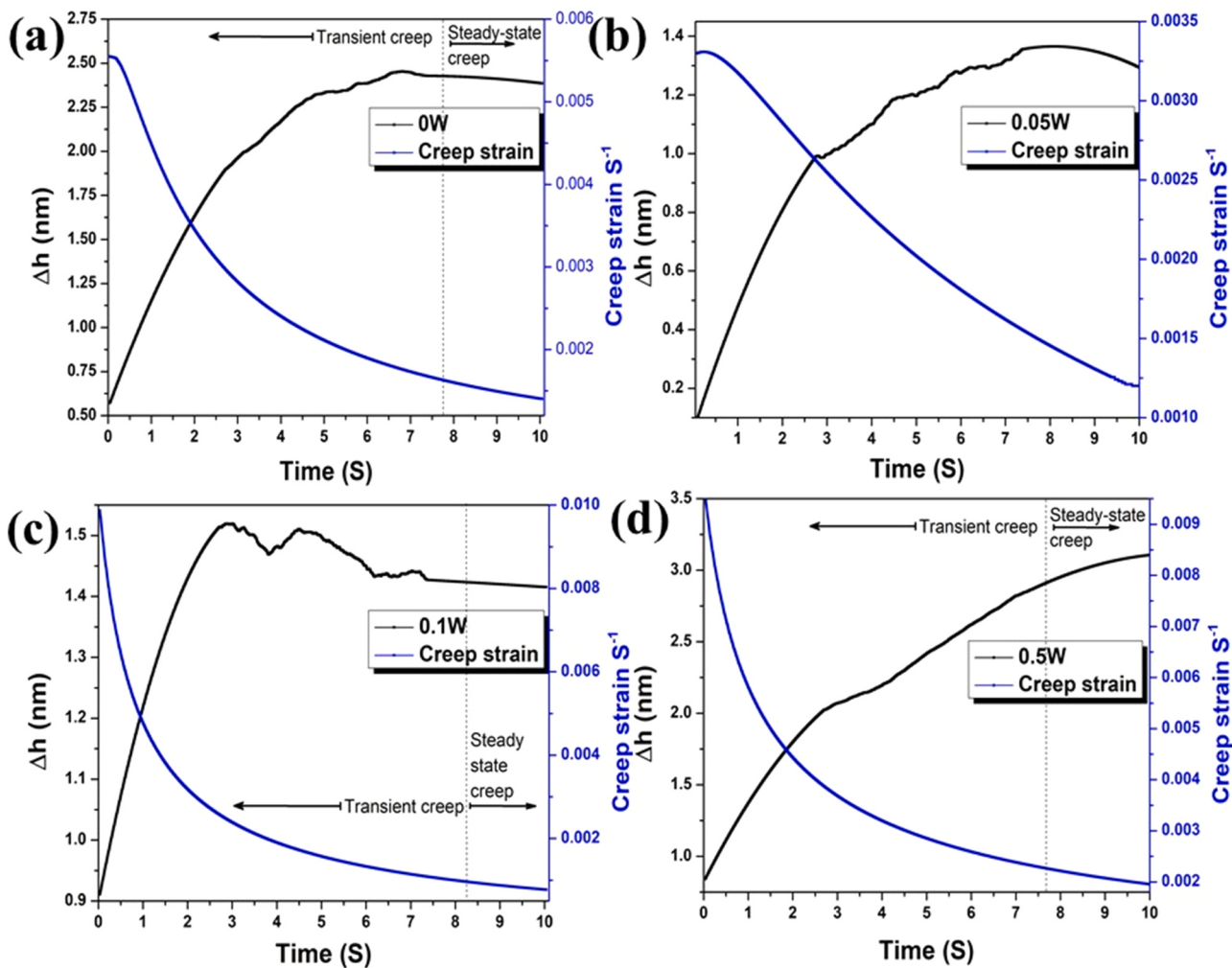


Fig. 8. Indentation creep performance of AlCrFeMnNiW<sub>x</sub> HEAs ( $x = 0, 0.05, 0.1$ , and  $0.5 \text{ mol}$ ).

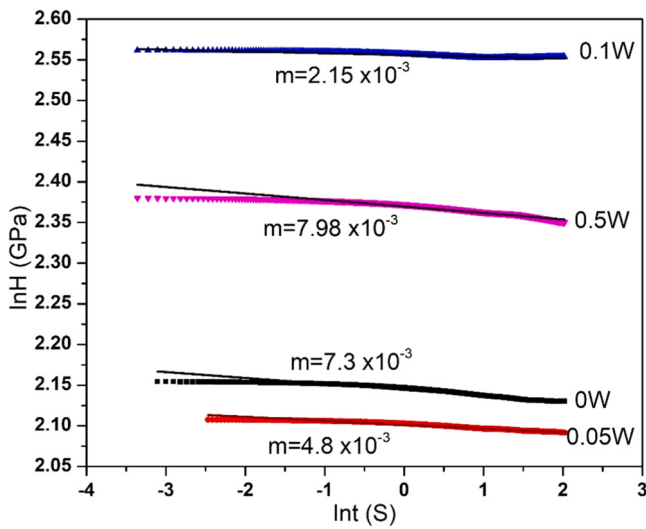


Fig. 9. Double logarithmic relationship between the hardness and time for AlCrFeMnNiW<sub>x</sub> HEAs ( $x = 0, 0.05, 0.1$ , and  $0.5 \text{ mol}$ ).

in this study, the 8–10–1 backpropagation model (8 neurons in the input layer, 10 neurons in the hidden layer, and 1 neuron in the output layer) was created. The entire modeling was performed and

implemented using the MATLAB (R2022b) program. A similar model has been trained and predicted the hardness of the HEAs which has an outstanding correlation result with the experimental data [62].

The dataset provided as input could be well simulated using the backpropagation model, which could also forecast the creep behavior during the indentation test. After several trials, the 8–10–1 model was chosen. The mean square error (MSE), the most important variable for accurate prediction outcomes, was used to choose the model, and the best validation performance at 1000 epoch is shown in Fig. 11(a).

The output of the ANN prediction model was compared with the experimental results to see how well the data matched. The ideal proposed model that was used to simulate the creep data point is presented in Fig. 10(b). Fig. 10(c) shows a comparison of the experiment's findings with the expected findings. The experimental outcomes and anticipated results are remarkably similar, with training, testing, and validation having R-values above 0.9999.

The creep displacement of AlCrFeMnNiW<sub>x</sub> HEAs ( $x = 0, 0.05, 0.1$ , and  $0.5 \text{ mol}$ ) was obtained experimentally and the ANN estimated results were in good agreement, as evident in Fig. 11. The slope and y-intercept of the fitted line should both be one for the best match, and clearly, the training, validation, and testing slope values exceed 0.9999. Thus, the 8–10–1 ANN model was used to forecast the creep behavior of the HEAs which showed a strong relationship between the experimental and modeling performance.

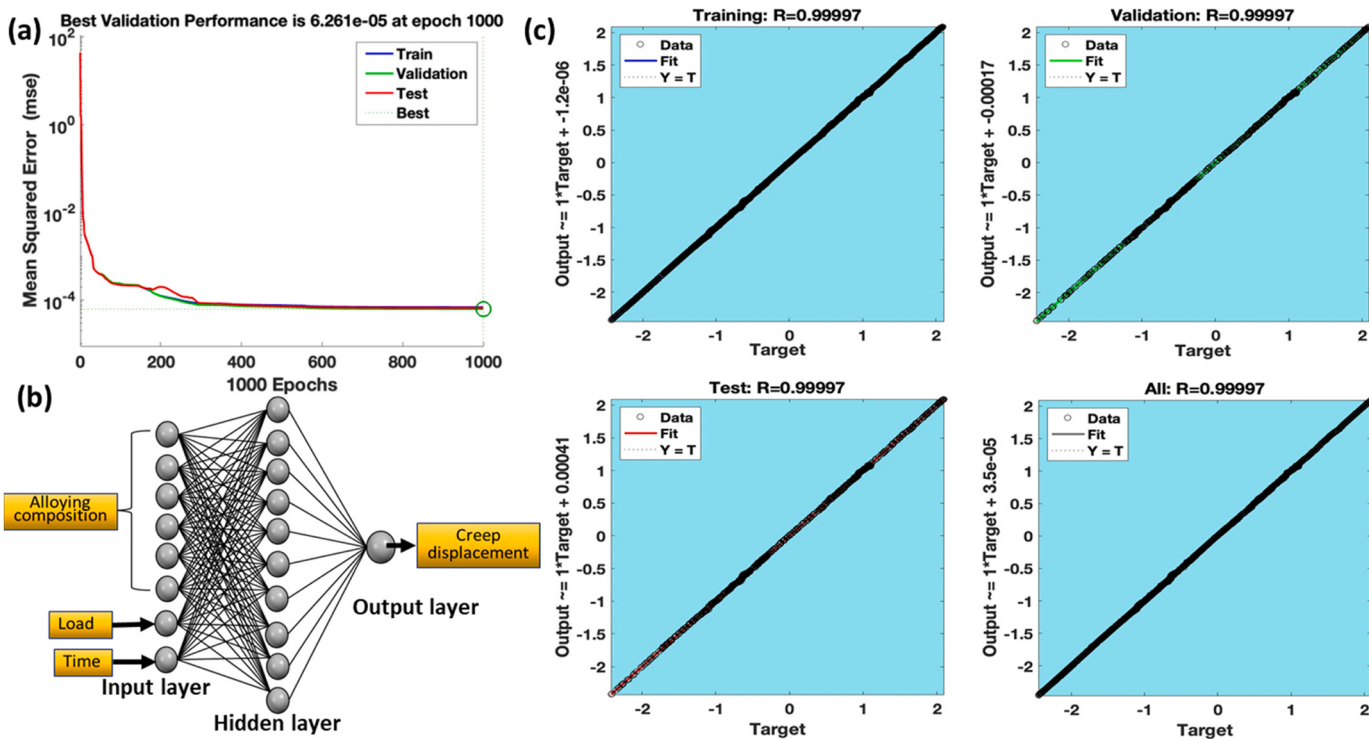


Fig. 10. (a) Best validation performance at the least MSE, (b) the proposed ANN model, and (c) regression analysis of the model's outcome.

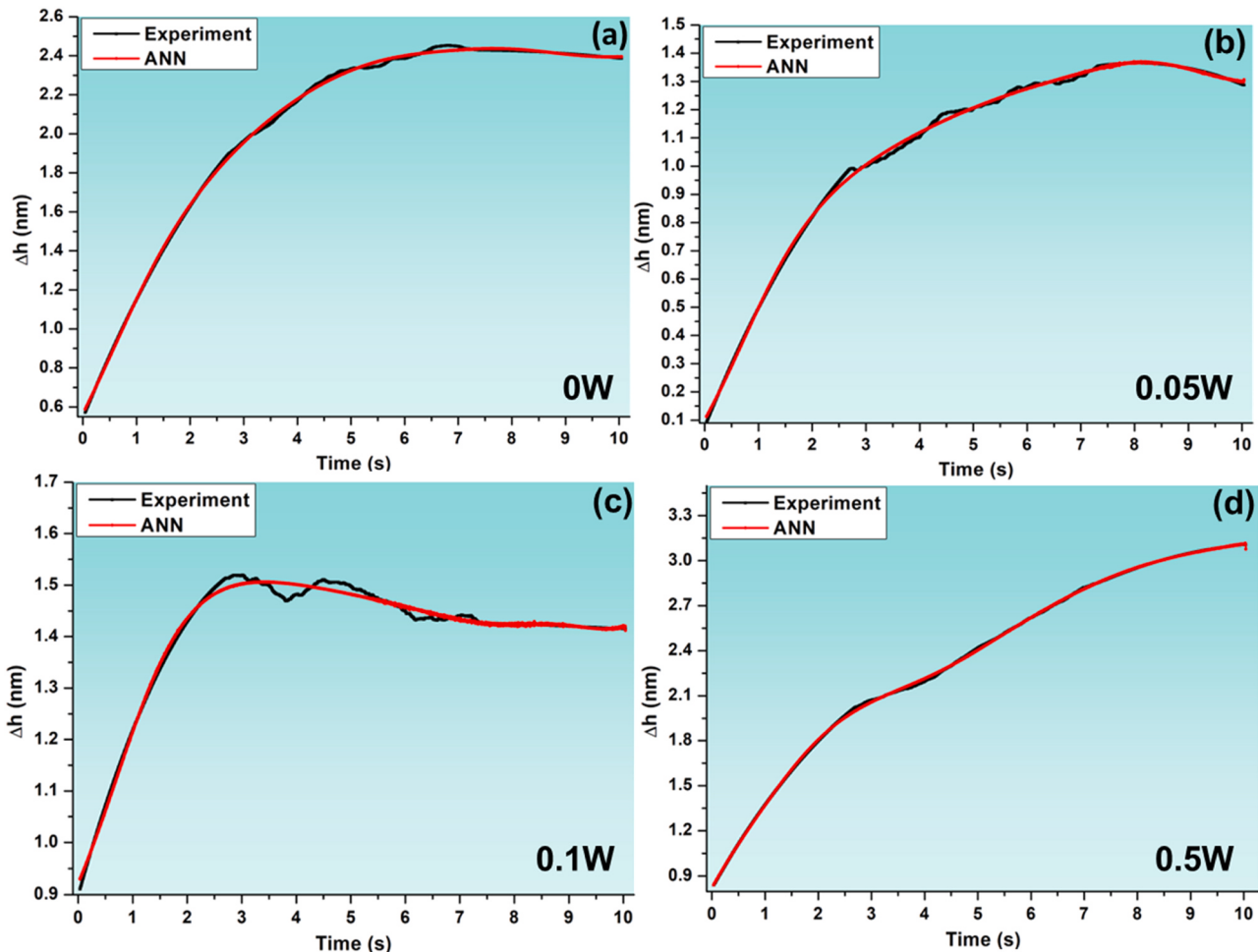


Fig. 11. Experimental creep behavior of AlCrFeMnNiW<sub>x</sub> ( $x = 0, 0.05, 0.1$ , and  $0.5$  mol) HEA with ANN prediction.

## 6. Conclusions

The following conclusions were drawn from the synthesis and characterization of AlCrFeMnNiW<sub>x</sub> HEAs ( $x = 0, 0.05, 0.1, 0.5$  mol).

- (1) The addition of the W element decreased the amount of the sigma ( $\sigma$ ) phase.
- (2) AlCrFeMnNiW<sub>x</sub> HEAs ( $x = 0, 0.05, 0.1, 0.5$  mol) have outstanding hardness values and modulus of elasticity owing to the presence of tungsten.
- (3) The HEA with  $x = 0.1$  exhibited excellent creep behavior during the investigation period at room temperature, signifying that the HEA is a suitable candidate for high-temperature and wear-resistant applications.
- (4) A predictive backpropagation ANN model was successively used for the prediction of creep behaviors, and its prediction showed high consistency with experimental data.
- (5) The ANN model showed that ANNs can be an effective tool for modeling and analysis. It could accurately predict ( $R > 0.9999$ ) creep behavior, which was verified through comparison with experimentally observed creep behavior. Thus, it could be used for process and product design.

## CRediT authorship contribution statement

**Sheetal Kumar Dewangan:** Conceptualization, Methodology, Validation, Investigation, Writing – original draft, Writing – review & editing, Funding acquisition. **Ashutosh Sharma:** Investigation, Resources, Writing – review & editing, Visualization, Supervision. **Hansung Lee:** Investigation, Writing – review & editing, Visualization. **Vinod Kumar:** Conceptualization, Resources, Writing – review & editing, Supervision. **Byungmin Ahn:** Conceptualization, Methodology, Writing – review & editing, Supervision, Project administration, Funding acquisition.

## Data Availability

The data that has been used is confidential. However, a sample data can be found in given link. <https://github.com/HEAresearch/creep>

## Declaration of Competing Interest

The authors declare that they have no known competing financial interests or personal relationships that could have appeared to influence the work reported in this paper.

## Acknowledgments

This work was supported by a National Research Foundation of Korea (NRF) grant funded by the Korean Government (MSIT) (Nos. 2021R1A2C1005478 and 2021R1A4A1031357). This research was also supported by the Basic Science Research Program through the National Research Foundation of Korea (NRF), funded by the Ministry of Education (No. 2022R111A1A01053047).

## References

- [1] ASM International Handbook Committee, ASM Handbook, Volume 07 - Powder Metal Technologies and Applications page, 1998. <https://doi.org/10.1007/s13398-014-0173-7>.
- [2] N. Li, F. Li, D. Gao, S. Yu, S. Zhang, H. Wang, Y. Chang, Effect of Zr addition on the microstructures and mechanical properties of ZrC–FeCrAl alloys, Mater. Sci. Eng., A 859 (2022) 144205, <https://doi.org/10.1016/J.MSEA.2022.144205>
- [3] U. Sunkari, S.R. Reddy, K.S. Athira, S. Chatterjee, P.P. Bhattacharjee, Effect of niobium alloying on the microstructure, phase stability and mechanical properties of CoCrFeNi2.1Nb high entropy alloys: Experimentation and thermodynamic modeling, Mater. Sci. Eng., A. 793 (2020) 139897, <https://doi.org/10.1016/J.MSEA.2020.139897>
- [4] S.K. Dewangan, Studies on microstructure, mechanical and high-temperature oxidation behaviour of tungsten containing high entropy alloys, Indian Institute of Technology Indore, 2021. <http://dspace.iiti.ac.in:8080/jspui/handle/123456789/3073> (accessed June 8, 2022).
- [5] T. Gu, L.M. Wang, Q. Hu, X.B. Liang, D.X. Fu, Y.X. Chen, X.M. Zhao, Y.W. Sheng, Effect of mechanical alloying and sintering behavior on the microstructure and properties of nbmotaure refractory high entropy alloy, Met. Mater. Int. (2022), <https://doi.org/10.1007/s12540-021-01165-6>
- [6] A. Sharma, H. Lee, B. Ahn, Effect of additive elements ( $x = \text{Cr, Mn, Zn, Sn}$ ) on the phase evolution and thermodynamic complexity of AlCuSiFe-x high entropy alloys fabricated via powder metallurgy, Met. Mater. Int. 28 (2022) 2216–2224, <https://doi.org/10.1007/s12540-021-01125-0>
- [7] X. Chen, D. Gao, J.X. Hu, Y. Liu, C.P. Tang, Evolution of microstructures and properties in AlxCrFeMn0.8Ni2.1 HEAs, Met. Mater. Int. 25 (2019) 1135–1144, <https://doi.org/10.1007/s12540-019-00282-7>
- [8] J.W. Yeh, S.K. Chen, S.J. Lin, J.Y. Gan, T.S. Chin, T.T. Shun, C.H. Tsau, S.Y. Chang, Nanostructured high-entropy alloys with multiple principal elements: Novel alloy design concepts and outcomes, +274, Adv. Eng. Mater. 6 (2004) 299–303, <https://doi.org/10.1002/adem.200300567>
- [9] D. Kumar, O. Maulik, S. Kumar, V.K. Sharma, Y.V.S.S. Prasad, V. Kumar, Impact of tungsten on phase evolution in nanocrystalline AlCuCrFeMnWx ( $x = 0, 0.05, 0.1$  and  $0.5$  mol) high entropy alloys, Mater. Res. Express 4 (2017) 114004, <https://doi.org/10.1088/2053-1591/aa96df>
- [10] S.K. Dewangan, V. Kumar, Application of artificial neural network for prediction of high temperature oxidation behavior of AlCrFeMnNiWx ( $X = 0, 0.05, 0.1, 0.5$ ) high entropy alloys, Int. J. Refract. Met. Hard Mater. 103 (2022) 105777, <https://doi.org/10.1016/j.ijrmhm.2022.105777>
- [11] O. Maulik, D. Kumar, S. Kumar, S. Dewangan, V. Kumar, Structure and properties of lightweight high entropy alloys: a brief review, Mater. Res. Express 5 (2018) 052001, <https://doi.org/10.1088/2053-1591/aabbca>
- [12] I. Moravcik, J. Cizek, P. Gavendova, S. Sheikh, S. Guo, I. Dlouhy, Effect of heat treatment on microstructure and mechanical properties of spark plasma sintered AlCoCrFeNiTi0.5high entropy alloy, Mater. Lett. 174 (2016) 53–56, <https://doi.org/10.1016/j.matlet.2016.03.077>
- [13] J. Li, H. Chen, Q. Fang, C. Jiang, Y. Liu, P.K. Liaw, Unraveling the dislocation–precipitate interactions in high-entropy alloys, Int. J. Plast. 133 (2020) 102819, <https://doi.org/10.1016/J.IJPLAS.2020.102819>
- [14] S. Varalakshmi, M. Kamaraj, B.S. Murty, Synthesis and characterization of nanocrystalline AlFeTiCrZnCu high entropy solid solution by mechanical alloying, J. Alloy. Compd. 460 (2008) 253–257, <https://doi.org/10.1016/j.jallcom.2007.05.104>
- [15] R. Anand Sekhar, S. Samal, N. Nayan, S.R. Bakshi, Microstructure and mechanical properties of Ti-Al-Ni-Co-Fe based high entropy alloys prepared by powder metallurgy route, J. Alloy. Compd. (2019) 123–132, <https://doi.org/10.1016/j.jallcom.2019.02.083>
- [16] A.I. Yurkova, V.V. Cherniavsky, V. Bolbut, M. Krüger, I. Bogomol, Structure formation and mechanical properties of the high-entropy AlCuNiFeCr alloy prepared by mechanical alloying and spark plasma sintering, J. Alloy. Compd. 786 (2019) 139–148, <https://doi.org/10.1016/j.jallcom.2019.01.341>
- [17] W. Chen, Z. Fu, S. Fang, H. Xiao, D. Zhu, Alloying behavior, microstructure and mechanical properties in a FeNiCrCo0.3Al0.7high entropy alloy, Mater. Des. 51 (2013) 854–860, <https://doi.org/10.1016/j.matedes.2013.04.061>
- [18] G. Han, K.P. Marimuthu, H. Lee, Evaluation of thin film material properties using a deep nanoindentation and ANN, Mater. Des. 221 (2022) 111000, <https://doi.org/10.1016/J.MATDES.2022.111000>
- [19] L. Zhang, P. Yu, H. Cheng, H. Zhang, H. Diao, Y. Shi, B. Chen, P. Chen, R. Feng, J. Bai, Q. Jing, M. Ma, P.K. Liaw, G. Li, R. Liu, Nanoindentation creep behavior of an Al0.3CoCrFeNi high-entropy alloy, Metall. Mater. Trans. A 47 (2016) 5871–5875, <https://doi.org/10.1007/s11661-016-3469-8>
- [20] T.K. Tsao, A.C. Yeh, C.M. Kuo, K. Kakehi, H. Murakami, J.W. Yeh, S.R. Jian, The high temperature tensile and creep behaviors of high entropy superalloy, Sci. Rep. 7 (2017) 1–9, <https://doi.org/10.1038/s41598-017-13026-7>
- [21] Z. Wang, S. Guo, Q. Wang, Z. Liu, J. Wang, Y. Yang, C.T. Liu, Intermetallics Nanoindentation characterized initial creep behavior of a high-entropy-based alloy CoFeNi, Intermetallics 53 (2014) 183–186, <https://doi.org/10.1016/j.intermet.2014.05.007>
- [22] D. Kumar, V. Kumar, Room temperature nanoindentation creep characteristics and strain rate sensitivity of AlCuCrFeMnWx high entropy alloys, SSRN Electron. J. (2019), <https://doi.org/10.2139/ssrn.3414015>
- [23] Y. Ma, G.J. Peng, D.H. Wen, T.H. Zhang, Nanoindentation creep behavior in a CoCrFeCuNi high-entropy alloy film with two different structure states, Mater. Sci. Eng., A 621 (2015) 111–117, <https://doi.org/10.1016/j.msea.2014.10.065>
- [24] Z. Xu, H. Zhang, W. Li, A. Mao, L. Wang, G. Song, Y. He, Microstructure and nanoindentation creep behavior of CoCrFeMnNi high-entropy alloy fabricated by selective laser melting, Addit. Manuf. 28 (2019) 766–771, <https://doi.org/10.1016/j.addma.2019.06.012>
- [25] P. Gong, J. Jin, L. Deng, S. Wang, J. Gu, K. Yao, X. Wang, A Room temperature nanoindentation creep behavior of TiZrHfBeCu (Ni) high entropy bulk metallic glasses, Mater. Sci. Eng., A. 688 (2017) 174–179, <https://doi.org/10.1016/j.msea.2017.01.094>
- [26] R. Goodall, T.W. Clyne, A critical appraisal of the extraction of creep parameters from nanoindentation data obtained at room temperature, Acta Mater. 54 (2006) 5489–5499, <https://doi.org/10.1016/j.actamat.2006.07.020>

- [27] T.H. Zhang, J.H. Ye, Y.H. Feng, Y. Ma, On the spherical nanoindentation creep of metallic glassy thin films at room temperature, *Mater. Sci. Eng., A* 685 (2017) 294–299, <https://doi.org/10.1016/j.msea.2017.01.018>
- [28] S. Sun, P. Gao, G. Sun, Z. Cai, J. Hu, S. Han, J. Lian, X. Liao, Nanostructuring as a route to achieve ultra-strong high- and medium-entropy alloys with high creep resistance, *J. Alloy. Compd.* 830 (2020) 154656, <https://doi.org/10.1016/j.jallcom.2020.154656>
- [29] Q. Fan, K. Gan, D. Yan, Z. Li, Nanoindentation creep behavior of diverse microstructures in a pre-strained interstitial high-entropy alloy by high-throughput mapping, *Mater. Sci. Eng., A* 856 (2022) 143988, <https://doi.org/10.1016/J.MSEA.2022.143988>
- [30] F. Liu, Z. Wang, Z. Wang, J. Zhong, X. Wu, Z. Qin, Z. Li, L. Tan, L. Zhao, L. Zhu, L. Jiang, L. Huang, L. Zhang, Y. Liu, High-throughput determination of interdiffusivity matrices in Ni-Al-Ti-Cr-Co-Mo-Ta-W multicomponent superalloys and their application in optimization of creep resistance, *Mater. Today Commun.* 24 (2020) 101018, <https://doi.org/10.1016/j.mtcomm.2020.101018>
- [31] W. Sun, Y. Jiang, G. Sun, J. Hu, T. Zhou, Z. Jiang, J. Lian, Nanoindentation creep behavior and its relation to activation volume and strain rate sensitivity of nanocrystalline Cu, *Mater. Sci. Eng., A* 751 (2019) 35–41, <https://doi.org/10.1016/J.MSEA.2019.02.027>
- [32] X. Wang, P. Gong, L. Deng, J. Jin, S. Wang, P. Zhou, Nanoindentation study on the room temperature creep characteristics of a senary Ti 16.7 Zr 16.7 Hf 16.7 Cu 16.7 Ni 16.7 Be 16.7 high entropy bulk metallic glass, *J. Non Cryst. Solids* 470 (2017) 27–37, <https://doi.org/10.1016/j.jnoncrysol.2017.04.041>
- [33] A.E. Mayer, V.S. Krasnikov, V. v Pogorelko, Dislocation nucleation in Al single crystal at shear parallel to (111) plane: molecular dynamics simulations and nucleation theory with artificial neural networks, *Int. J. Plast.* 139 (2021) 102953, <https://doi.org/10.1016/J.IJPLAS.2021.102953>
- [34] F.T. Latypov, E. v Fomin, V.S. Krasnikov, A.E. Mayer, Dynamic compaction of aluminum with nanopores of varied shape: MD simulations and machine-learning-based approximation of deformation behavior, *Int. J. Plast.* 156 (2022) 103363, <https://doi.org/10.1016/J.IJPLAS.2022.103363>
- [35] S. Park, J.H. Fonseca, K.P. Marimuthu, C. Jeong, S. Lee, H. Lee, Determination of material properties of bulk metallic glass using nanoindentation and artificial neural network, *Intermetallics* 144 (2022) 107492, <https://doi.org/10.1016/J.INTERMET.2022.107492>
- [36] S. Laxmikant Vajire, A. Prashant Singh, D. Kumar Saini, A. Kumar Mukhopadhyay, K. Singh, D. Mishra, Novel machine learning-based prediction approach for nanoindentation load-deformation in a thin film: Applications to electronic industries, *Comput. Ind. Eng.* 174 (2022) 108824, <https://doi.org/10.1016/J.CIE.2022.108824>
- [37] C. Nagarjuna, S.K. Dewangan, A. Sharma, K. Lee, S.-J. Hong, B. Ahn, Application of artificial neural network to predict the crystallite size and lattice strain of CoCrFeMnNi high entropy alloy prepared by powder metallurgy, *Met. Mater. Int.* 29 (2022) 1968–1975, <https://doi.org/10.1007/s12540-022-01355-w>
- [38] Z. Savaedi, R. Motallebi, H. Mirzadeh, A review of hot deformation behavior and constitutive models to predict flow stress of high-entropy alloys, *J. Alloy. Compd.* 903 (2022) 163964, <https://doi.org/10.1016/J.JALLCOM.2022.163964>
- [39] O. Ibragimova, A. Brahme, W. Muhammad, J. Lévesque, K. Inal, A new ANN based crystal plasticity model for FCC materials and its application to non-monotonic strain paths, *Int. J. Plast.* 144 (2021) 103059, <https://doi.org/10.1016/J.IJPLAS.2021.103059>
- [40] U. Ali, W. Muhammad, A. Brahme, O. Skiba, K. Inal, Application of artificial neural networks in micromechanics for polycrystalline metals, *Int. J. Plast.* 120 (2019) 205–219, <https://doi.org/10.1016/J.IJPLAS.2019.05.001>
- [41] D.B. Miracle, M.H. Tsai, O.N. Senkov, V. Soni, R. Banerjee, Refractory high entropy superalloys (RSAs), *Scr. Mater.* 187 (2020) 445–452, <https://doi.org/10.1016/J.scriptamat.2020.06.048>
- [42] O. Senkov, D. Isheim, D. Seidman, A. Pilchak, Development of a refractory high entropy superalloy, *Entropy* 18 (2016) 102, <https://doi.org/10.3390/e18030102>
- [43] Y. Dong, Y. Lu, Effects of tungsten addition on the microstructure and mechanical properties of near-eutectic AlCoCrFeNi<sub>2</sub> high-entropy alloy, *J. Mater. Eng. Perform.* 27 (2018) 109–115, <https://doi.org/10.1007/s11665-017-3096-6>
- [44] S.K. Dewangan, D. Kumar, S. Samal, V. Kumar, Microstructure and mechanical properties of nanocrystalline AlCrFeMnNiW<sub>x</sub> ( $x = 0, 0.05, 0.1, 0.5$ ) high-entropy alloys prepared by powder metallurgy route, *J. Mater. Eng. Perform.* (2021), <https://doi.org/10.1007/s11665-021-05552-3>
- [45] D. Kumar, O. Maulik, A.S. Bagri, Y.V.S.S. Prasad, V. Kumar, Microstructure and characterization of mechanically alloyed equiatomic AlCuCrFeMnW high entropy alloy, *Mater. Today Proc.* 3 (2016) 2926–2933, <https://doi.org/10.1016/j.matpr.2016.09.005>
- [46] S.K. Dewangan, V.K. Sharma, P. Sahu, V. Kumar, Synthesis and characterization of hydrogenated novel AlCrFeMnNiW high entropy alloy, *Int. J. Hydrog. Energy* 45 (2020) 16984–16991, <https://doi.org/10.1016/j.ijhydene.2019.08.113>
- [47] S. Guo, C. Ng, J. Lu, C.T. Liu, Effect of valence electron concentration on stability of fcc or bcc phase in high entropy alloys, *J. Appl. Phys.* 109 (2011) 103505, <https://doi.org/10.1063/1.3587228>
- [48] A.K. Singh, N. Kumar, A. Dwivedi, A. Subramaniam, A geometrical parameter for the formation of disordered solid solutions in multi-component alloys, *Intermetallics* 53 (2014) 112–119, <https://doi.org/10.1016/j.intermet.2014.04.019>
- [49] S.K. Dewangan, S. Samal, V. Kumar, Microstructure exploration and an artificial neural network approach for hardness prediction in AlCrFeMnNiW<sub>x</sub> High-Entropy Alloys, *J. Alloy. Compd.* 823 (2020) 153766, <https://doi.org/10.1016/J.JALLCOM.2020.153766>
- [50] W.C. Oliver, G.M. Pharr, Measurement of hardness and elastic modulus by instrumented indentation: advances in understanding and refinements to methodology, *J. Mater. Res.* 19 (2004) 3–20, <https://doi.org/10.1557/jmr.2004.19.1.3>
- [51] J. Li, B. Gao, Y. Wang, X. Chen, Y. Xin, S. Tang, B. Liu, Y. Liu, M. Song, Microstructures and mechanical properties of nano carbides reinforced CoCrFeMnNi high entropy alloys, *J. Alloy. Compd.* 792 (2019) 170–179, <https://doi.org/10.1016/j.jallcom.2019.03.403>
- [52] J. Wang, B. Liu, C.T. Liu, Y. Liu, Strengthening mechanism in a high-strength carbon-containing powder metallurgical high entropy alloy, *Intermetallics* 102 (2018) 58–64, <https://doi.org/10.1016/j.intermet.2018.07.016>
- [53] S. Guo, L. Jiang, H. Kang, Z. Cao, B. Wen, Y. Dong, Y. Lu, H. Ruan, T. Li, Z. Wang, J. Jie, T. Wang, A Promising New Class of High-Temperature Alloys: Eutectic High-Entropy Alloys, *Sci. Rep.* 4 (2014) 1–5, <https://doi.org/10.1038/srep06200>
- [54] M.H. Tsai, K.Y. Tsai, C.W. Tsai, C. Lee, C.C. Juan, J.W. Yeh, Criterion for sigma phase formation in Cr- and V-Containing high-entropy alloys, *Mater. Res. Lett.* 1 (2013) 207–212, <https://doi.org/10.1080/21663831.2013.831382>
- [55] R.S. Ganji, P. Sai Karthik, K. Bhanu Sankara Rao, K.V. Rajulapati, Strengthening mechanisms in equiatomic ultrafine grained AlCoCrCuFeNi high-entropy alloy studied by micro- and nanoindentation methods, *Acta Mater.* 125 (2017) 58–68, <https://doi.org/10.1016/j.actamat.2016.11.046>
- [56] Z. Xu, H. Zhang, W. Li, A. Mao, L. Wang, G. Song, Y. He, Microstructure and nanoindentation creep behavior of CoCrFeMnNi high-entropy alloy fabricated by selective laser melting, *Addit. Manuf.* 28 (2019) 766–771, <https://doi.org/10.1016/j.addma.2019.06.012>
- [57] M.F. Doerner, W.D. Nix, A method for interpreting the data from depth-sensing indentation instruments, 1986, *J. Mater. Res.* 1 (1986) 601–609.
- [58] L. Zhang, P. Yu, H. Cheng, H. Zhang, H. Diao, Y. Shi, B. Chen, P. Chen, R. Feng, J. Bai, Q. Jing, M. Ma, P.K. Liaw, G. Li, R. Liu, Nanoindentation creep behavior of an Al0.3CoCrFeNi high-entropy alloy, *Metall. Mater. Trans. A* 47 (2016) 5871–5875, <https://doi.org/10.1007/s11661-016-3469-8>
- [59] Y. Zhao, X. Wang, T. Cao, J.-K. Han, M. Kawasaki, J. Jang, H.N. Han, U. Ramamurty, L. Wang, Y. Xue, Effect of grain size on the strain rate sensitivity of CoCrFeNi high-entropy alloy, *Mater. Sci. Eng., A* 782 (2020) 139281, <https://doi.org/10.1016/j.msea.2020.139281>
- [60] P. Gong, S. Wang, F. Li, X. Wang, Alloying effect on the room temperature creep characteristics of a Ti-Zr-Be bulk metallic glass, *Phys. B: Phys. Condens. Matter* 530 (2018) 7–14, <https://doi.org/10.1016/j.physb.2017.11.029>
- [61] J. Qiu, G. Xiao, T. Jin, B. Su, X. Shu, S. Ma, Indentation strain rate sensitivity of CoCrFeNiAl 0.3 high-entropy alloy, *Adv. Eng. Mater.* 21 (2019) 1–5, <https://doi.org/10.1002/adem.201800744>
- [62] R. Jain, S.K. Dewangan, V. Kumar, S. Samal, Artificial neural network approach for microhardness prediction of eight component FeCoNiCrMnVAlNb eutectic high entropy alloys, *Mater. Sci. Eng.: A* 797 (2020) 140059, <https://doi.org/10.1016/j.msea.2020.140059>